2188 *Biochemistry* **1989**, *28*, 2188–2198

Determination of the Three-Dimensional Solution Structure of the Antihypertensive and Antiviral Protein BDS-I from the Sea Anemone *Anemonia sulcata*: A Study Using Nuclear Magnetic Resonance and Hybrid Distance Geometry–Dynamical Simulated Annealing[†]

Paul C. Driscoll,[‡] Angela M. Gronenborn,*[,‡] Laszlo Beress,[§] and G. Marius Clore*[,‡]

Laboratory of Chemical Physics, National Institute of Diabetes and Digestive and Kidney Diseases, National Institutes of Health, Bethesda, Maryland 20892, and Abteilung Toxikologie, Klinikum der Christian-Albrechts-Universität, Hospitalstrasse 4-6, D2300 Kiel, West Germany

Received June 24, 1988; Revised Manuscript Received September 22, 1988

ABSTRACT: The three-dimensional solution structure of the antihypertensive and antiviral protein BDS-I from the sea anemone *Anemonia sulcata* has been determined on the basis of 489 interproton and 24 hydrogen-bonding distance restraints supplemented by 23 ϕ backbone and 21 χ_1 side-chain torsion angle restraints derived from nuclear magnetic resonance (NMR) measurements. A total of 42 structures is calculated by a hybrid metric matrix distance geometry–dynamical simulated annealing approach. Both the backbone and side-chain atom positions are well defined. The average atomic rms difference between the 42 individual SA structures and the mean structure obtained by averaging their coordinates is 0.67 ± 0.12 Å for the backbone atoms and 0.90 ± 0.17 Å for all atoms. The core of the protein is formed by a triple-stranded antiparallel β-sheet composed of residues 14–16 (strand 1), 30–34 (strand 2), and 37–41 (strand 3) with an additional mini-antiparallel β-sheet at the N-terminus (residues 6–9). The first and second strands of the triple-stranded antiparallel β-sheet are connected by a long exposed loop (residues 17–30). A number of side-chain interactions are discussed in light of the structure.

In the preceding paper (Driscoll et al., 1989) we presented the sequential and stereospecific assignment of the ^{1}H NMR[1] spectrum of BDS-I, a small protein from the sea anemone *Anemonia sulcata* with both antihypertensive and antiviral properties (Beress et al., 1985). Although at the present time the mechanism of action of BDS-I with respect to either of its two activities is unknown, it is clear that the determination of the three-dimensional structure of this protein will be essential to an understanding of its biological and pharmacological properties.

In recent years a number of structures of proteins in solution have been determined by nuclear magnetic resonance (NMR) spectroscopy [see Wüthrich (1986) and Clore and Gronenborn (1987) for reviews]. Comparison with X-ray structures has shown that the overall polypeptide fold can be reasonably well defined (Williamson et al., 1985; Kline et al., 1986; Wagner et al., 1987; Clore et al., 1986a, 1987a,b,c,d). The precision, however, with which the structures have been determined to date, as measured by the atomic rms difference between the individual structures and the mean structure obtained by averaging their coordinates, has been of the order of 1–2 Å for the backbone atoms and 1.5–3 Å for all atoms. One approach to improve the precision of such structure determinations lies in extracting a larger number of structural restraints from the NMR data. In particular, stereospecific assignment of methylene proton resonances, as well as the increased sensitivity offered by 600-MHz spectrometers, should enable a larger number of interproton distances to be obtained. With this goal in mind, we present the determination of the three-dimensional structure of BDS-I, on the basis of the sequential and stereospecific assignments presented in the preceding paper (Driscoll et al., 1989). A set of 489 approximate interproton distance restraints, 23 ϕ backbone torsion angle restraints, and 21 χ_1 side-chain torsion angle restraints are derived from the NOESY, DQF-COSY, HOHAHA, and E-COSY spectra. These restraints, together with 12 backbone hydrogen bonds deduced from a qualitative interpretation of the NOEs and NH exchange rates, provide the experimental data for the three-dimensional structure calculations using the hybrid distance geometry–dynamical simulated annealing approach (Nilges et al., 1988a). A total of 42 structures are computed, and the average atomic rms difference between the individual structures and the mean structure obtained by averaging their coordinates is 0.67 ± 0.12 Å for the backbone atoms and 0.90 ± 0.17 Å for all atoms.

EXPERIMENTAL PROCEDURES

Sample Preparation and NMR. Sample preparation and NMR spectroscopy were carried out as described in the preceding paper (Driscoll et al., 1989).

Calculations. Three-dimensional structures were calculated on the basis of the NMR data with the hybrid metric matrix distance geometry–dynamical simulated annealing approach (Nilges et al., 1988a,b). The metric matrix distance geometry

---

[†] This work was supported by the Intramural AIDS Targeted Antiviral Program of the Office of the Director of the National Institutes of Health and Grant 321/4003/0318909A from the Bundesministerium für Forschung und Technologie (G.M.C and A.M.G.)

[‡] National Institutes of Health.

[§] Klinikum der Christian-Albrechts-Universität.

[1] Abbreviations: NMR, nuclear magnetic resonance; NOE, nuclear Overhauser effect; NOESY, two-dimensional NOE spectroscopy; DQF-COSY, double quantum filtered correlated spectroscopy; E-COSY, exclusive correlated spectroscopy; HOHAHA, two-dimensional homonuclear Hartmann–Hahn spectroscopy; rms, root mean square; SA, simulated annealing

0006-2960/89/0428-2188$01.50/0

part of the calculations was carried out with the program DISGEO (Havel et al., 1979, 1983; Havel & Wüthrich, 1985; Havel, 1986). The dynamical simulated annealing calculations were carried out with the program XPLOR (Brünger, 1988; Brünger et al., 1986, 1987a,b), which is derived originally from the program CHARMM (Brooks et al., 1983) and has been especially adapted for restrained molecular dynamics and dynamical simulated annealing calculations (Clore et al., 1985, 1986b; Nilges et al., 1988a,b,c). All computations were carried out on either MicroVAXII, VAX8550, or CONVEX C1-XP computers.

RESULTS AND DISCUSSION

Experimental Restraints. BDS-I is an approximately 1:1 mixture of two forms, differing in the amino acid at position 18: (Leu-18)-BDS-I and (Phe-18)-BDS-I. As no qualitative difference in the pattern of NOEs or coupling constants for the two forms of BDS-I could be detected, we conclude that the structures of the two species are identical within the precision of the NOE and coupling constant data and of the accuracy of the present structure calculations. Consequently, all structure calculations were restricted to (Leu-18)-BDS-I. The calculations were based on a collection of interproton, hydrogen-bond, and disulfide bridge distance restraints supplemented by ϕ backbone, χ_1 side-chain, and proline ω peptide bond torsion angle restraints.

A set of 489 structurally useful NOEs consisting of 150 short- ($|i-j| \leq 5$) and 105 long- ($|i-j| > 5$) range interresidue NOEs together with 234 intraresidue NOEs were first identified in the 120- and 200-ms NOESY spectra. These were then classified into three distance ranges, 1.8–2.7, 1.8–3.3, and 1.8–5.0 Å, corresponding to strong, medium, and weak NOEs, respectively, on the basis of the 50- and 120-ms NOESY data. The upper limits of distances involving methyl and methylene protons, as well as the $C^{\delta}H$ and $C^{\epsilon}H$ protons of Phe and Tyr, were corrected for center $\langle r_c \rangle$ averaging (which is equivalent to the use of pseudoatoms) as described by Wüthrich et al. (1983). For all NOEs involving methyl groups, an additional 0.5 Å per methyl group was added to the upper distance limit to account for the higher intensity of the resonances (Wagner et al., 1987; Clore et al., 1987b). It should be noted that although spin diffusion may contribute to the intensity of some of the very weak peaks in the 120-ms mixing time NOESY spectra, it is easily calculated that, for a protein of the size of BDS-I, even indirect NOEs will not be detectable beyond ~5 Å. Consequently, the distance classification used is sufficiently loose to ensure that the possible inclusion of indirect NOE effects does *not* result in the introduction of errors into the structure calculations.

In addition to the NOE distance restraints, 24 supplementary distance restraints corresponding to backbone NH–CO hydrogen bonds were also included in the input distance restraint list. These were identified according to the criteria laid out by Wagner et al. (1987), which comprise the presence of NOEs between residues on opposite strands of an antiparallel β-sheet in conjunction with a slowly exchanging backbone NH proton. Of the 21 slowly exchanging backbone NH protons identified in Figure 5 of the preceding paper (Driscoll et al., 1989), 12 could be assigned unambiguously in this manner to hydrogen bonds within antiparallel β-sheet segments. These NH(i)–CO(j) hydrogen bonds were as follows: (i,j) = (6,9), (9,6), (13,4), (14,40), (40,14), (16,38), (37,34), (32,39), (39,32), and (41,30), where i and j represent the residue positions of the two amino acids involved. The distance ranges used to constrain the hydrogen bonds were $r_{N(i)-O(j)} \leq 3.3$ Å and $r_{NH(i)-O(j)} \leq 2.3$ Å.

Further distance constraints were used in the distance geometry phase of some of the calculations (see below) to define three disulfide bridges between Cys-4 and Cys-39, Cys-6 and Cys-32, and Cys-22 and Cys-40. These are $r_{C\beta(i)-S(j)} = 2.99 \pm 0.05$ Å and $r_{S(i)-S(j)} = 2.02 \pm 0.05$ Å. The disulfide links were identified by model building with the readily identifiable secondary structure elements deduced from the pattern of short-range and certain long-range NOEs involving the NH, $C^{\alpha}H$, and $C^{\beta}H$ protons (Driscoll et al., 1989). Explicitly, a triple-stranded antiparallel β-sheet containing about 50% of the protein sequence and including Cys-32, Cys-39, and Cys-40 (see below) was identified at an early stage (Driscoll et al., 1989). The positions of the side chains of these cysteines precluded the formation of disulfide bridges between themselves. A disulfide bridge between Cys-4 and Cys-6 was also eliminated on steric grounds since these residues are separated by only two positions in the chain. Positive identification of two of the three disulfide linkages was then derived from the following NOEs: the NOEs from Cys-39 $C^{\beta}H$ to Ala-2 $C^{\beta}H_3$ and from Cys-39 $C^{\beta}H$ to Cys-4 $C^{\beta}H$ define a disulfide bridge between Cys-4 and Cys-39, and the NOE between Cys-40 $C^{\beta}H$ and Cys-22 $C^{\beta}H$ defines the disulfide bridge between Cys-22 and Cys-40. The disulfide bridge between Cys-6 and Cys-32 was thus identified by elimination. Confirmation of the correct assignment of disulfide bridges was obtained by the results of distance geometry calculations (see below). Additionally, the pattern of disulfide linkages deduced from NMR data for BDS-I is identical with that determined chemically for the homologous *Anemonia sulcata* toxin ATX-II (Wunderer, 1978).

Restraints for the ϕ backbone torsion angles of 23 residues were derived from ${}^3J_{HN\alpha}$ coupling constants (Pardi et al., 1984). In particular, the 20 residues with ${}^3J_{HN\alpha} > 8$ Hz were restrained to the range $-80° \leq \phi \leq -160°$, while the three with ${}^3J_{HN\alpha} < 7$ Hz were restrained to the range $-40° \leq \phi \leq -85°$ [see Figure 5 of Driscoll et al. (1989)]. Restraints for the χ_1 side-chain torsion angles of 21 non-proline residues were derived on the basis of ${}^3J_{\alpha\beta}$ coupling constants and intraresidue NOEs as described by Wagner et al. (1987). Eight χ_1 angles were restrained to the range $0° \leq \chi_1 \leq 120°$, four to the range $120° \leq \chi_1 \leq 240°$, seven to the range $-120° \leq \chi_1 \leq 0°$, and two to the range $0 \leq \chi_1 \leq 240°$ [see Figure 5 in Driscoll et al. (1989)]. Finally, for *cis*-prolines Pro-36 and Pro-42 the ω torsion angle was constrained to $0 \pm 5°$ and for the remaining *trans*-prolines to $180 \pm 5°$ [see Driscoll et al. (1989) for identification of *cis*-prolines].

The complete list of all experimental restraints used in the computations is available as supplementary material (see paragraph at end of paper regarding supplementary material).

Tertiary Structure Computation. Computation of the tertiary structure of BDS-I was carried out according to the hybrid distance geometry–dynamical simulated annealing method of Nilges et al. (1988a).

The first stage of this procedure is based on a metric matrix distance geometry algorithm operating in n-dimensional distance space (Crippen & Havel, 1978; Havel et al., 1979, 1983) and makes use of the program DISGEO (Havel & Wüthrich, 1984; Havel, 1986). [Note that n is given by $N(N-1)/2$, where N is the number of atoms.] Briefly, this involves randomly generating a set of distance values between a subset of atoms (comprising the N, C, C^{α}, $C^{\alpha}H$, C^{β}, and nonterminal C^{γ} and C^{δ} atoms and a pseudoatom for the aromatic rings) which lie within the distance bounds imposed by all the experimental restraints, the complete covalent geometry and the hard sphere atomic van der Waals radii, followed by projection from multidimensional distance space into three-dimensional Cartesian coordinate space to yield a "substructure". As the randomly chosen distances are not checked with respect to the triangle inequalities, this procedure takes only a small amount of computational time (~5 min on a VAX8550 computer). The coordinates of the substructures are an approximation to those of the complete structures consistent with all the data and are used as the starting point for the subsequent calculations. It should be noted, however, that the substructures have very poor nonbonded contacts and fail to satisfy a large number of experimental interproton distance restraints with an average of more than 100 violations greater than 0.5 Å.

The second stage involves the application of a protocol of dynamical simulated annealing (Nilges et al., 1988a,b,c) in real Cartesian coordinate space. This is similar in spirit to restrained molecular dynamics (Clore et al., 1985, 1986a,b; Brünger et al., 1986, 1987a,b; Kaptein et al., 1985) in that it involves solving Newton's equations of motion for all atoms of the system for a suitable time at a temperature which is directly proportional to the kinetic energy of the system. It differs, however, from restrained molecular dynamics in one very important respect. Namely, all the nonbonded interaction terms of the usual empirical energy function are replaced by a simple van der Waals repulsion term. This not only speeds up the calculations but increases computational flexibility and avoids the introduction of any potential bias arising from contributions of the empirical energy function. Thus, the target function is similar to that employed by other methods such as metric matrix distance geometry (Crippen & Havel, 1978; Havel, 1986), and restrained least-squares minimization in torsion angle space with either a variable target function (Braun & Go, 1985) or a sequence of ellipsoids of constantly decreasing volume, each of which contains the minimum of the target function (Billeter et al., 1987).

The total target function, which in effect represents the potential energy of the system (whose units are kcal·mol^{-1}), is made up of the following terms:

$$F_{\text{tot}} = F_{\text{covalent}} + F_{\text{repel}} + F_{\text{NOE}} + F_{\text{tor}} \quad (1)$$

F_{covalent} is the target function for maintaining correct bond lengths, angles, chirality, and planes and is given by

$$F_{\text{covalent}} = \sum_{\text{bonds}} k_{\text{b}}(r - r_0)^2 + \sum_{\text{angles}} k_\theta(\theta - \theta_0)^2 + \sum_{\text{impropers}} k_\omega(\omega - \omega_0)^2 \quad (2)$$

The values chosen for the force constants for the bond (k_{b}), angle (k_θ), and improper torsions (k_ω) are set to uniform high values to ensure near perfect stereochemistry thoughout the calculations, namely, 600 kcal·mol^{-1}·Å^{-2}, 500 kcal·mol^{-1}·rad^{2}, and 500 kcal·mol^{-1}·rad^{-2}, respectively. (Note that the improper torsions serve to maintain planarity and chirality, and with the exception of prolines, the conformation about the peptide bonds is assumed to be planar and trans.)

F_{repel} is the target function used to prevent unduly close nonbonded contacts and is given by

$$F_{\text{repel}} = \begin{cases} 0 & \text{if } r \geq sr_{\text{min}} \\ k_{\text{vdw}}(s^2 r_{\text{min}}{}^2 - r^2)^2 & \text{if } r < sr_{\text{min}} \end{cases} \quad (3)$$

The values of r_{min} are the standard values of the van der Waals radii as represented by the Lennard-Jones van der Waals radii used in the CHARMM empirical energy function (Brooks et al., 1983). The van der Waals radius scale factor s is set to 0.8 in the present calculations, and the resulting hard sphere van der Waals radii are similar to those used in various other distance geometry programs (Havel, 1986; Braun & Go, 1985; Billeter et al., 1987).

Table I: Protocol Used for the Dynamical Simulated Annealing Calculations

phase 1	200 cycles Powell minimization k_{NOE} = 0 kcal·mol^{-1}·Å^{-2} k_{tor} = 0 kcal·mol^{-1}·rad^{-1} k_{rep} = 0.1 kcal·mol^{-1}·Å^{-4} [a]
phase 2	3.75-ps dynamics at 1000 K [b] k_{NOE} = 1 → 50 kcal·mol^{-1}·Å^{-2} [c] k_{tor} = 5 → 200 kcal·mol^{-1}·rad^{-2} [c] k_{rep} = 0.01 → 4.0 kcal·mol^{-1}·Å^{-4} [a,d]
phase 3	1.5-ps dynamics at 300 K [e] k_{NOE} = 50 kcal·mol^{-1}·Å^{-2} k_{tor} = 200 kcal·mol^{-1}·rad^{-2} k_{rep} = 4 kcal·mol^{-1}·Å^{-4} [a]
phase 4	200 cycles of Powell minimization k_{NOE} = 50 kcal·mol^{-1}·Å^{-2} k_{tor} = 200 kcal·mol^{-1}·rad^{-2} k_{rep} = 4 kcal·mol^{-1}·Å^{-4} [a]

[a] The scale factor s for the van der Waals radii used to calculate the van der Waals repulsion term, F_{repel}, given by eq 3 is 0.8. [b] The initial velocities in phase 2 are assigned to a Maxwellian distribution at 1000 K, and the velocities are then rescaled every 75 fs to 1000 K. The step size for the integrator is 1 fs. [c] The values of the force constants k_{NOE} and k_{tor} for the square-well potentials (cf. eq 4 and 5) for the NOE (F_{NOE}) and torsion angle (F_{tor}) restraints are increased every 75 fs by doubling their values until they reach the maximum value indicated. [d] The value for the force constant k_{rep} for the van der Waals repulsion term F_{repel} is increased every 75 fs by multiplying its value by $400^{1/50}$. [e] The velocities in phase 3 are rescaled every 150 fs to 300 K.

F_{NOE} and F_{tor} are the target functions for the NOE and torsion angle restraints and are represented by square-well potentials of the form (Clore et al., 1986a)

$$F_{\text{NOE}} = \begin{cases} k_{\text{NOE}}(r_{ij} - r_{ij}{}^{\text{u}})^2 & \text{if } r_{ij} > r_{ij}{}^{\text{u}} \\ 0 & \text{if } r_{ij}{}^{\text{l}} \leq r_{ij} \leq r_{ij}{}^{\text{u}} \\ k_{\text{NOE}}(r_{ij} - r_{ij}{}^{\text{l}})^2 & \text{if } r_{ij} < r_{ij}{}^{\text{l}} \end{cases} \quad (4)$$

and

$$F_{\text{tor}} = \begin{cases} k_{\text{tor}}(\varphi_i - \varphi_i{}^{\text{u}})^2 & \text{if } \varphi_i > \varphi_i{}^{\text{u}} \\ 0 & \text{if } \varphi_i{}^{\text{l}} \leq \varphi_i \leq \varphi_i{}^{\text{u}} \\ k_{\text{tor}}(\varphi_i - \varphi_i{}^{\text{l}})^2 & \text{if } \varphi_i < \varphi_i{}^{\text{l}} \end{cases} \quad (5)$$

where k_{NOE} and k_{tor} are variable force constants, $r_{ij}{}^{\text{u}}$ and $\varphi_i{}^{\text{u}}$ are the upper limits for the distance and torsion angle restraints, respectively, and $r_{ij}{}^{\text{l}}$ and $\varphi_i{}^{\text{l}}$ are the corresponding lower limits. The lower limit of the interproton distance restraints is set to 1.8 Å, approximately the sum of the hard sphere van der Waals radii of two protons; closer approach of the respective proton pairs is also prevented by the van der Waals repulsion term F_{repel} (eq 3).

The starting coordinates for the dynamical simulated annealing calculations are obtained by best fitting one residue at a time to the subset of atoms present in the substructures and subjecting the resulting coordinates to 200 cycles of Powell minimization to regularize the peptide bond. This is followed by the protocol of dynamical simulated annealing (Nilges et al., 1988a) given in Table I to yield the final SA structures. Each SA structure took ~1 h to compute on a VAX8550 computer, and the average backbone atomic rms shifts produced by dynamical simulated annealing were of the order of 2.0–2.5 Å for the backbone atoms and 3.0–3.5 Å for all atoms.

A total of 50 substructures, 25 with disulfide restraints and 25 without, were calculated in stage 1 of the calculations. Of these, 47 had the same global polypeptide fold, and the remaining 3 were mirror images of the former. (Note that the mirror images are easily detected as they have D- instead of L-amino acids.) The observation that the incorporation of disulfide restraints had no effect on the resulting fold confirms the disulfide bridge assignments made on the basis of the NOE data. Unambiguous confirmation was obtained by examining the substructures on an interactive graphics display which

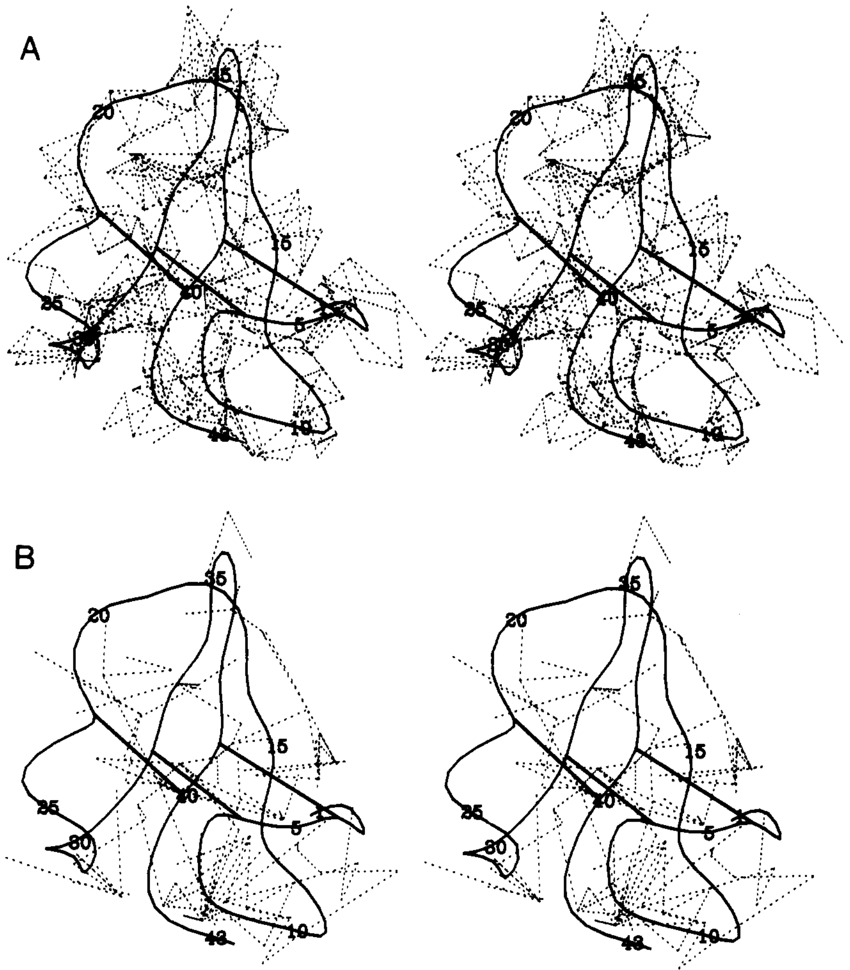

FIGURE 1: (A) Intraresidue and short-range interresidue ($|i-j| \leq 5$) and (B) the long-range interresidue ($|i-j| > 5$) interproton distance restraints shown as dashed lines superimposed on a framework comprising a smoothed backbone (N, C^α, C) atom representation of the restrained minimized average structure $(\overline{\text{SA}})$r. The three disulfide bridges between residues 4 and 39, 6 and 32, and 22 and 40 are shown as straight lines connecting the corresponding C^α atoms.

revealed that our disulfide assignments were the only ones consistent with the backbone conformation. Consequently, the restraints for the three disulfide bridges were included in the bond and angle terms of F_{covalent} (cf. eq 1 and 2) in the subsequent dynamical simulated annealing calculations. In stage 2, the 47 substructures with the correct chirality were subjected to dynamical simulated annealing. This resulted in 42 structures which satisfied the experimental restraints with no interproton distance violations greater than 0.5 Å. The other five SA structures all had a number of violations greater than 0.5 Å, as well as some poor nonbonded contacts. It should be noted that in terms of atomic rms differences the latter structures lie within the distribution of the former. In each case, however, the violations could be attributed to specific problems of local geometry. Consequently, we restricted all further analysis to the former 42 SA structures.

As described previously (Clore et al., 1986b), the coordinates of the 42 final SA structures were best fitted to each other and averaged to yield the mean structure $\overline{\text{SA}}$. The poor stereochemistry and nonbonded contacts of the mean structure were easily corrected by 1000 cycles of restrained minimization with only minor atomic rms shifts to generate the structure $(\overline{\text{SA}})$r. This structure is closer to the mean structure than any of the individual SA structures, while satisfying the experimental restraints as well as any of the individual structures.

Converged Structures. The structural statistics for the 42 SA structures, as well as for the mean structure $\overline{\text{SA}}$ and the restrained minimized mean structure $(\overline{\text{SA}})$r, are given in Table II. All 42 SA structures, as well as the $(\overline{\text{SA}})$r structure, satisfy the experimental restraints, display very small deviations from idealized covalent geometry, and have good nonbonded contacts as evidenced by small values of F_{repel} and negative Lennard-Jones van der Waals energies.

The overall polypeptide fold is illustrated in Figures 1 and 2, which show the superposition of the interproton distance restraints on a smooth backbone representation of the $(\overline{\text{SA}})$r structure and the best fit superposition of the backbone (N, C^α, C) atoms of all 42 SA structures, respectively. It is evident from Figure 2, as well as from the atomic rms differences given in Table III and the plot of the atomic rms distribution of the SA structures as a function of residue shown in Figure 3, that the backbone fold of BDS-I is exceptionally well determined. This is reflected by the very small value for the average backbone atomic rms difference between the individual SA structures and the mean structure $\overline{\text{SA}}$, only 0.67 ± 0.12 Å, as well as by the small deviations in the ϕ and ψ angles (Figure 4). We also note that all the non-glycine residues lie within the allowed region of the Ramachandran ϕ, ψ plot (Figure 5).

The main secondary structure feature of BDS-I is a triple-stranded antiparallel β-sheet, which is observed to possess a large degree of right-handed twist (when defined in terms of the twist of the hydrogen-bonding direction or of the peptide planes as viewed along a strand). This is in agreement with crystallographic findings which have shown that most β-pleated

Table II: Structural Statistics[a]

	⟨SA⟩	$\overline{SA}$	$(\overline{SA})r$
rms deviations from experimental restraints (Å)[b]			
all (513)	0.085 ± 0.002	0.059	0.079
interresidue short range ($\|i - j\| \leq 5$) (150)	0.083 ± 0.005	0.053	0.086
interresidue long range ($\|i - j\| > 5$) (105)	0.111 ± 0.007	0.082	0.100
intraresidue (234)	0.074 ± 0.006	0.053	0.065
hbond (24)[c]	0.051 ± 0.010	0.038	0.043
F_{NOE} (kcal·mol^{-1})[d]	187 ± 11	92	160
F_{tor} (kcal·mol^{-1})[e]	26 ± 6	13	24
F_{repel} (kcal·mol^{-1})[f]	91 ± 7	2417	72
F_{L-J} (kcal·mol^{-1})[g]	−103 ± 11	$>10^6$	−117
deviations from idealized geometry[h]			
bonds (Å) (646)	0.014 ± 0.006	0.329	0.013
angles (deg) (1157)	2.910 ± 0.363	28.373	2.517
impropers (deg) (242)	0.830 ± 0.060	2.629	0.797

[a] The notation of the structures is as follows: ⟨SA⟩ are the 42 final dynamical simulated annealing structures; $\overline{SA}$ is the mean structure obtained by averaging the coordinates of the 42 individual SA structures best fitted to each other; $(\overline{SA})r$ is the structure obtained by restrained minimization of $\overline{SA}$. [b] The rms deviations from the experimental restraints are calculated with respect to the upper and lower limits of the distance restraints (Clore et al., 1986a). None of the structures exhibited violations greater than 0.5 Å. The number of distances in each category is given in parentheses next to the category name. [c] For each backbone hydrogen bond there are two restraints: $r_{NH-O} < 2.3$ Å and $r_{N-O} < 3.3$ Å. The lower limits are given by the sum of the van der Waals radii of the relevant atoms. 12 backbone hydrogen bonds within regular elements of secondary structure were identified on the basis of the NOE and NH exchange data [see text and Driscoll et al. (1989)]. [d] The values of the square-well NOE potential F_{NOE} (eq 4) are calculated with a force constant of 50 kcal·mol^{-1}·Å^{-2}. [e] The values of F_φ are calculated with a force constant of 200 kcal·mol^{-1}·rad^{-2}. F_φ is a square-well dihedral potential (eq 5) which is used to restrict the ranges of 23 ϕ and 21 χ_1 torsion angles as indicated in Figure 5 of Driscoll et al. (1979) and the ω peptide bond torsion angles of the five proline residues (Pro-36 and -42 being restrained to the cis conformation and the others to the trans; see text). [f] The values of the van der Waals repulsion term F_{repel} (cf. eq 3) are calculated with a force constant of 4 kcal·mol^{-1}·Å^{-4} with the hard sphere van der Waals radii set to 0.8 times the standard values used in the CHARMM empirical energy function (Brooks et al., 1983). [g] F_{L-J} is the Lennard-Jones van der Waals energy calculated with the CHARMM empirical energy function (Brooks et al., 1983). [h] The number of bond, angle, and improper terms is given in parentheses. The improper terms serve to maintain planarity and appropriate chirality; they also maintain the peptide bond of all residues (with the exception of prolines) in the trans conformation. In the dynamical simulated annealing calculations, the restraints for the disulfide bridges are included in the bond and angle terms.

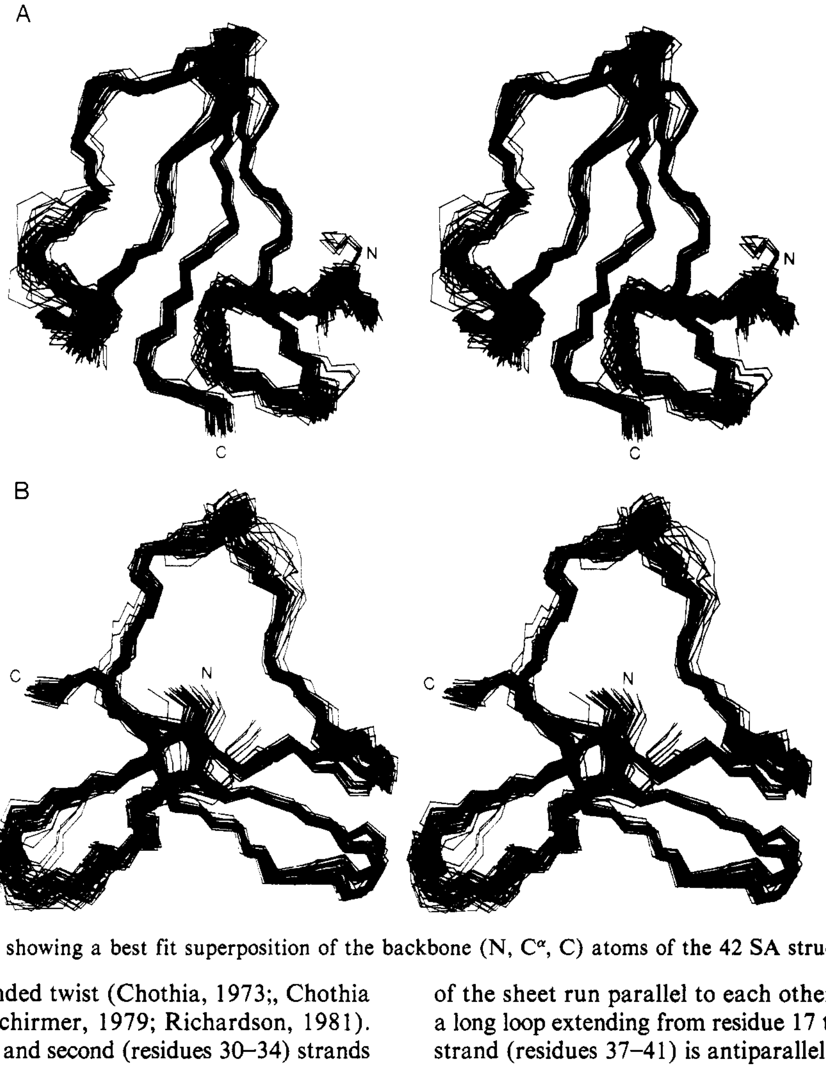

FIGURE 2: Two stereoviews showing a best fit superposition of the backbone (N, C$^\alpha$, C) atoms of the 42 SA structures.

sheets contain a right-handed twist (Chothia, 1973;, Chothia et al., 1977; Schulz & Schirmer, 1979; Richardson, 1981). The first (residues 14–16) and second (residues 30–34) strands of the sheet run parallel to each other and are connected by a long loop extending from residue 17 to residue 30. The third strand (residues 37–41) is antiparallel to and lies between the

Table III: Atomic rms Differences[a]

	atomic rms difference (Å)	
structures	backbone atoms	all atoms
$\langle SA \rangle$ vs $\overline{SA}$[b]	0.67 ± 0.12	0.90 ± 0.17
$\langle SA \rangle$ vs $\langle SA \rangle$[b]	0.96 ± 0.19	1.29 ± 0.23
$\langle SA \rangle$ vs $(\overline{SA})r$	0.73 ± 0.13	1.00 ± 0.18
$(\overline{SA})r$ vs $\overline{SA}$	0.21	0.45

[a] The notation of the structures is the same as that in Table II.
[b] Note that by use of standard statistical theory it is easily shown that the average rms difference between all pairs of SA structures is related to the average rms difference between the individual SA structures and the mean $\overline{SA}$ structure by a factor of $\sim[2n/(n-1)]^{1/2}$, which in this case is equal to 1.43. Further, the standard atomic rms error s_{mean} in the coordinates of the average mean structure $\overline{SA}$ is given by $[\sum(\text{rmsd}_i)^2/n(n-1)]^{1/2}$, where rmsd_i is the atomic rms difference between the ith SA structure and the mean $\overline{SA}$ structure and n is the number of structures. The values for s_{mean} are 0.13 and 0.15 Å for the backbone atoms and all atoms, respectively.

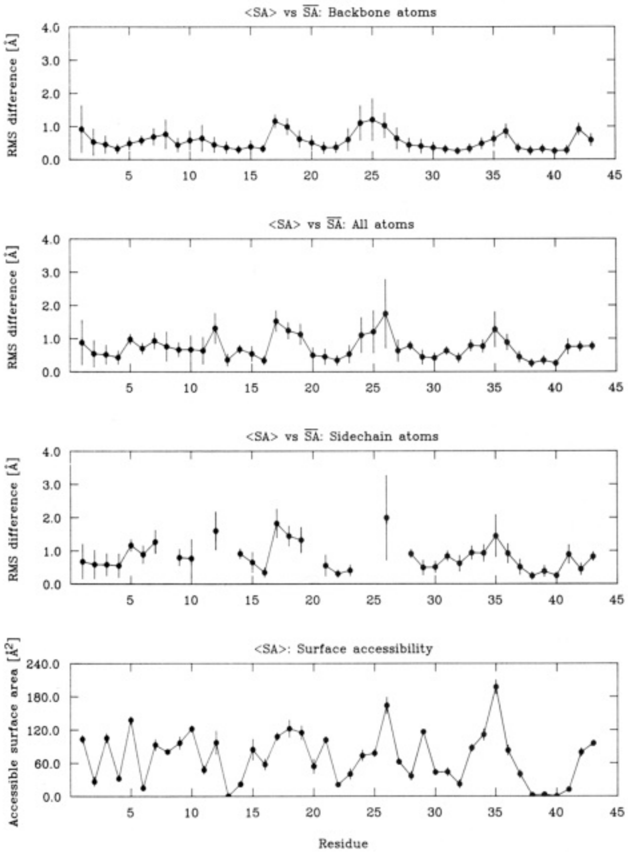

FIGURE 3: Atomic rms distribution of the 42 individual SA structures about the mean structure $\overline{SA}$ best fitted to residues 1–43 and surface accessibility. The filled-in circles (●) represent the average rms difference at each residue between the individual structures and the mean structure, and the bars represent the standard deviations in these values; similar representation is used for the surface accessibility.

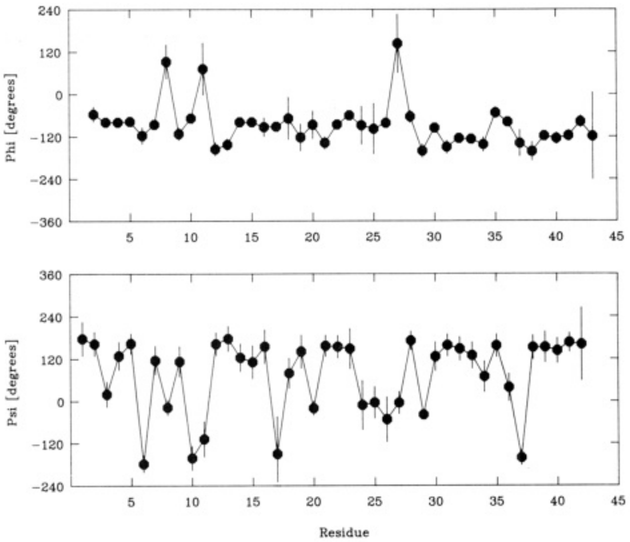

FIGURE 4: Angular rms distribution of the ϕ and ψ backbone torsion angles of the 42 SA structures. The closed circles (●) are the values of the ϕ and ψ angles of the restrained minimized mean structure $(\overline{SA})r$, and the bars represent the average angular rms deviations between all pairs of SA structures.

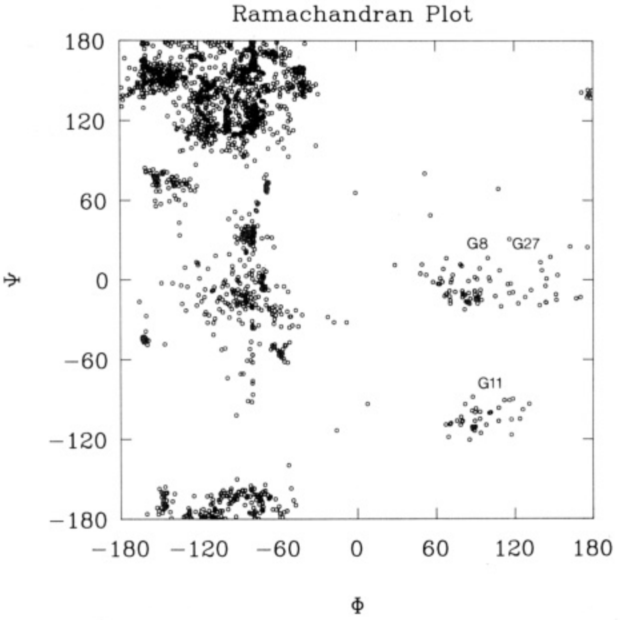

FIGURE 5: Ramachandran ϕ, ψ plot for the 42 SA structures. All non-glycine residues lie within the allowed region of ϕ, ψ phase space (Schulz & Schirmer, 1979; Richardson, 1981).

other two strands, forming backbone hydrogen bonds to them. The second and third strands of the β-sheet are connected by a classical type VIa turn from residue 34 to residue 37 with Pro-36 in the cis conformation, ϕ, ψ angles of $(-52 \pm 15^\circ, 157 \pm 32^\circ)_{35}$ and $(-79 \pm 6^\circ, 39 \pm 38^\circ)_{36}$, and a hydrogen bond between Asn-37 NH and Lys-34 CO [see Richardson (1981) for a classification of tight turns]. The other element of regular secondary structure consists of a mini-antiparallel β-sheet and a classical type II turn extending from residue 6 to residue 9 with ϕ, ψ angles of $(-91 \pm 7^\circ, 110 \pm 40^\circ)_7$ and $(101 \pm 47^\circ, -29 \pm 21^\circ)_8$ and a hydrogen bond between Lys-9 NH and Cys-6 CO. Residues 4 and 13 are also hydrogen bonded in an antiparallel fashion. Residues 10–12 form a bulge opposite residue 5. The hydrogen bonding within the secondary structure elements is illustrated by the superpositions shown in Figure 6. Finally, a type VIb turn is formed by residues 40–43 with Pro-42 in the cis conformation and ϕ, ψ angles of $(-118 \pm 15^\circ, 166 \pm 35^\circ)_{41}$ and $(-78 \pm 17^\circ, 161 \pm 27^\circ)$. For this turn, however, no NH$(i + 3)$–CO(i) backbone hydrogen bond was observed.

The conformation of the long loop (residues 17–30) is also well defined. This is due to the presence of numerous long-range NOEs between the side chains of residues 18, 21, 22, and 28 on the one hand and residues in strand 3 on the other, as well as between residue 28 and residues in strand 1 (Figure 1B), supplemented by a high density of short-range NOEs within the loop (Figure 1A). Indeed only two regions are not quite as well defined as the antiparallel β-sheet, namely, the tight turn leading from strand 1 to the loop (residues 17–19)

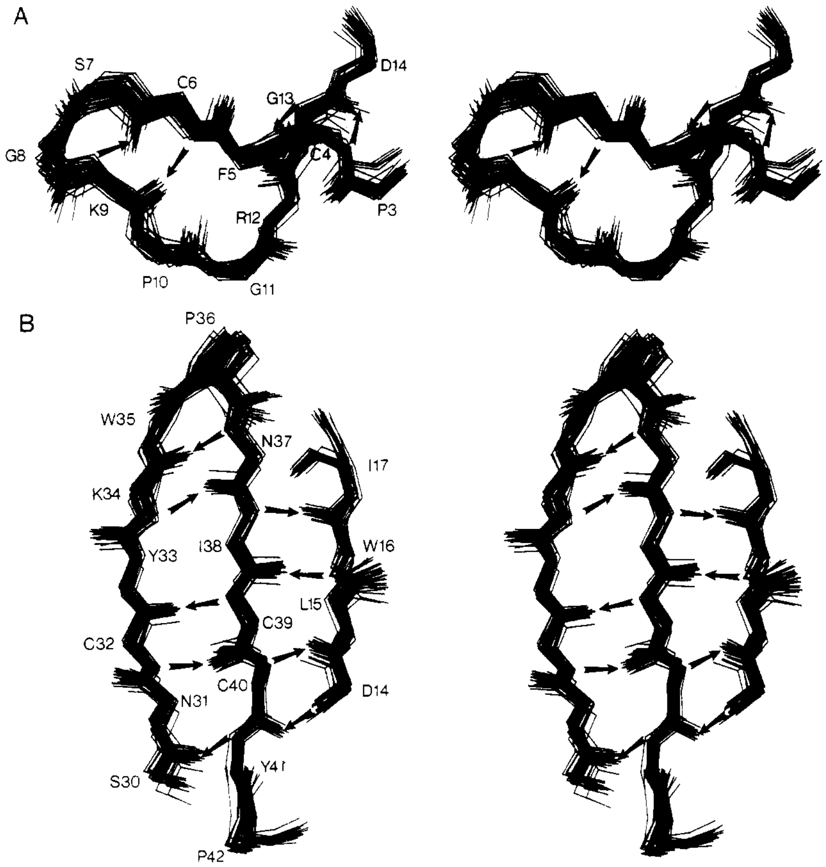

FIGURE 6: Stereoviews showing best fit superpositions of the backbone (N, C^α, C, O) atoms of the 42 SA structures for the two regions of regular secondary structure. Backbone hydrogen bonds are shown as arrows with the direction of the arrow from the N to the O atom. (A) Residues 3–14; (B) residues 14–17 and 30–42.

which appears to be clustered around two conformations and the most exposed region of the loop comprising residues 24–26 (Figure 2). This is associated with a larger variability of the following backbone torsion angles: ψ_{17} and ϕ_{18} in the case of residues 17–19 and ψ_{24}, ϕ_{25}, ψ_{26}, and ϕ_{27} in the case of residues 24–26 (Figure 4). For the latter, the variability may be due in part to our inability to stereospecifically assign the $C^\alpha H$ protons of glycines-24, -25, and -27.

In general, side-chain positions cannot be defined quite as well as those of the backbone atoms. Although this general trend is also true of BDS-I, most of the side-chain positions are actually well determined. The average atomic rms difference between the individual 42 SA structures and the mean $\overline{\text{SA}}$ structure is only 0.90 ± 0.17 Å for all atoms, just 0.2 Å larger than that for the backbone atoms. Further, only 8 out of the 36 side chains have atomic rms distribution values above 1 Å (Figure 3). Without exception these 8 side chains lie on the surface of the protein and display the largest surface accessiblities. Just how well defined side-chain positions can be is illustrated in Figure 7 which shows best fit superpositions of some selected regions of the protein. It should be appreciated that the definition of the side-chain positions is directly related to the number of NOE distance restraints to them, as well as to the presence or absence of χ_1 torsion angle restraints. This is particularly evident for long side chains such as Arg and Lys. For example, Arg-19 is well defined up to the C^γ position, but as no NOEs were detected involving the $C^\delta H$, $N^\epsilon H$, or guanidinium group, these atoms are poorly defined (Figure 7C).

The high degree of accuracy (Figures 3 and 7) with which the side chains are determined for BDS-I allows a rationalization of some of their properties in the NMR spectrum. For example, the aromatic side chains of Tyr-28, observed to be slowly flipping on the NMR time scale (Driscoll et al., 1988), and Trp-16 are juxtaposed in a manner that suggests a hydrogen bond between the $N^{\epsilon1}H$ proton of Trp-16 and the hydroxyl oxygen atom of Tyr-28 [$r_{N\epsilon1(16)-O\eta(28)} \sim 2.7$ Å and angle $N^{\epsilon1}(16)$–$N^{\epsilon1}H(16)$–$O^\eta(28) \sim 172°$; see Figures 7B and 8B]. In addition, the close contacts of the Tyr-28 ring with the side chains of Trp-16, Tyr-26, and Pro-23 may provide some restriction to its movement (Figure 8B). Associated with the close proximity of Pro-23 to these aromatic residues is the significant upfield shift of the resonances associated with its $C^\gamma H_2$ (−0.29 and 0.58 ppm) and $C^\delta H_2$ (2.41 and 2.52 ppm) groups. Note that the position of the aromatic ring of Tyr-26 is not well determined (Figures 3 and 8B). This is hardly surprising as Tyr-26 lies in the center of the long loop and has one of the highest surface accessibilities in the protein (Figure 3) so that its orientation is not restricted in any way by internal packing requirements. Further, only three interresidue NOEs involving the aromatic ring of Tyr-26 were observed (namely, between Tyr-26 $C^\delta H$ and Tyr-28 $C^\epsilon H$ and between Tyr-26 $C^\delta H$ and $C^\epsilon H$ on the one hand and Pro-23 $C^\gamma H$ on the other).

The relative orientation of Tyr-41 and His-43 (Figure 7C) suggests a hydrogen bond between the His-43 $N^{\delta1}H$ and the hydroxyl oxygen atom of Tyr-41 [$r_{N\delta1(43)-O\delta(41)} \sim 2.6$ Å and angle $N^{\delta1}(43)$–$N^{\delta1}H(43)$–$O^\eta(41) \sim 140°$]. Such an interaction is supported by the observation of an elevated pK_a of His-43 (pK_a ~7.9). As His-43 is a surface residue with a high surface accessibility (Figure 3), one would expect a pK_a of ~6.7 in the absence of a hydrogen-bonding or salt bridge interaction (Markley, 1975).

It is of interest to highlight the location and nature of the charged residues of this cationic polypeptide. The protein

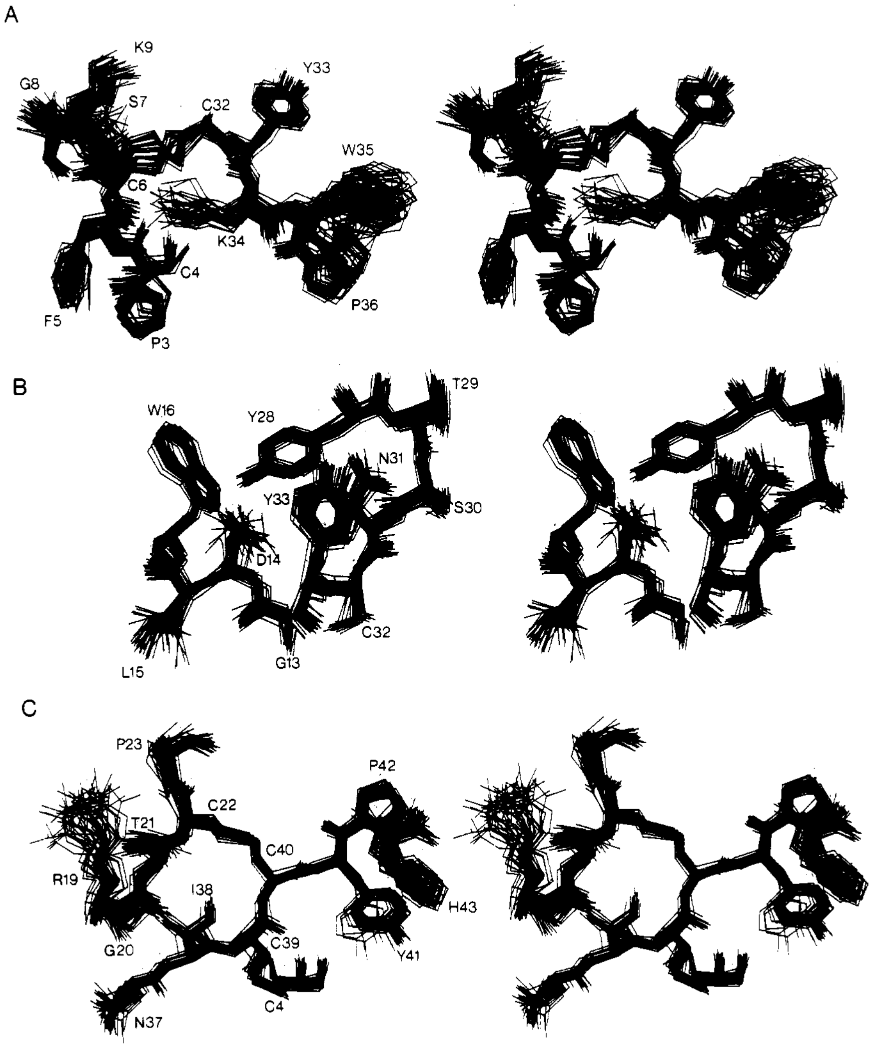

FIGURE 7: Stereoviews showing best fit superposition of all atoms (excluding protons) of the 42 SA structures for three selected segments of the protein. (A) Residues 3–9 and 32–36, (B) residues 13–16 and 28–33, and (C) residues 4, 19–22, and 37–43.

contains one acidic residue, Asp-14, and four basic residues, Arg-12 and -19 and Lys-9 and -34. The positively charged groups are not found to be clustered together to form any sort of recognition patch but are found in relatively isolated positions. For example, the side chain of Lys-9 lies along the surface of the protein with the aliphatic hydrocarbon portion in contact with the buried side chain of Tyr-41 (Figure 8A). The arrangement of these two side chains nicely explains the relatively high-field chemical shifts of the $C^{\gamma}H_2$ and $C^{\delta}H_2$ groups of Lys-9 (0.23 and 0.52 ppm and 0.87 ppm, respectively). The side chains of Arg-19 and Lys-34 are directed away from the surface of the protein. As discussed above, the charged terminus of the arginine side chain is relatively poorly determined (Figure 7C). A single long-range NOE between the $N^{\zeta}H_3^+$ protons of Lys-34 and the $C^{\alpha}H$ proton of Cys-6 is sufficient to position the Lys-34 side chain in the converged structures (Figure 7A and 8B). A likely rationale for the location of this residue is a hydrogen bond between the $N^{\zeta}H_3^+$ group and the carbonyl oxygen atom of Phe-5 [$r_{N\zeta(34)-O(5)} \sim$ 3.2 Å and angle $N^{\zeta}(34)-N^{\zeta}H(34)-O(5) \sim 124°$].

Figure 8A shows that in the majority of the converged structures the guanidinium group of Arg-12 is brought within close range of the side chain of Asp-14. Also within close proximity of the acidic group is the N-terminal NH_3^+ group of Ala-1. The possible formation of a salt bridge in this region of the protein was probed by recording a series of 2D HOHAHA spectra in H_2O between pH 1.0 and pH 6.5. The advantage of the HOHAHA experiment is that, with a sufficiently long mixing time, it is possible to follow the pH-dependent chemical shifts of both labile and nonlabile protons in one experiment via the observation of the intraresidue multiple relayed connectivities. This study revealed no dramatic chemical shift changes save for the NH, $C^{\alpha}H$, and $C^{\beta}H$ resonances of residue His-43, which can be attributed to the titration of the free C-terminal carboxyl group. Between pH 1.5 and pH 1.0, however, small but significant shifts (0.2 ppm) of the amide NH protons of Asp-14 and Gly-13 and the $N^{\epsilon}H$ proton of Arg-12 were observed, suggesting a concerted pH-dependent conformational change in this part of the protein. This is probably due to the protonation of the Asp-14 side chain; the pH range of the changes observed suggests that the pK_a of this group is depressed below 1.5, indicative of a salt bridge.

We note in passing that the point of heterogeneity in the BDS-I primary structure at position 18 in the sequence is located in an exposed region at the start of the long loop between residues 17 and 30 (Figure 3). The high surface accessibility of Leu-18 in the converged structures is consistent with the absence of interresidue NOEs for this residue's side chain in the NMR spectra of either (Leu-18)- or (Phe-18)-BDS-I. Likewise, the localization of the largest chemical shift differences between the two forms of the protein to stretches of the protein chain between residues 15–21 and 33–37 is readily explained on the basis of the three-dimensional

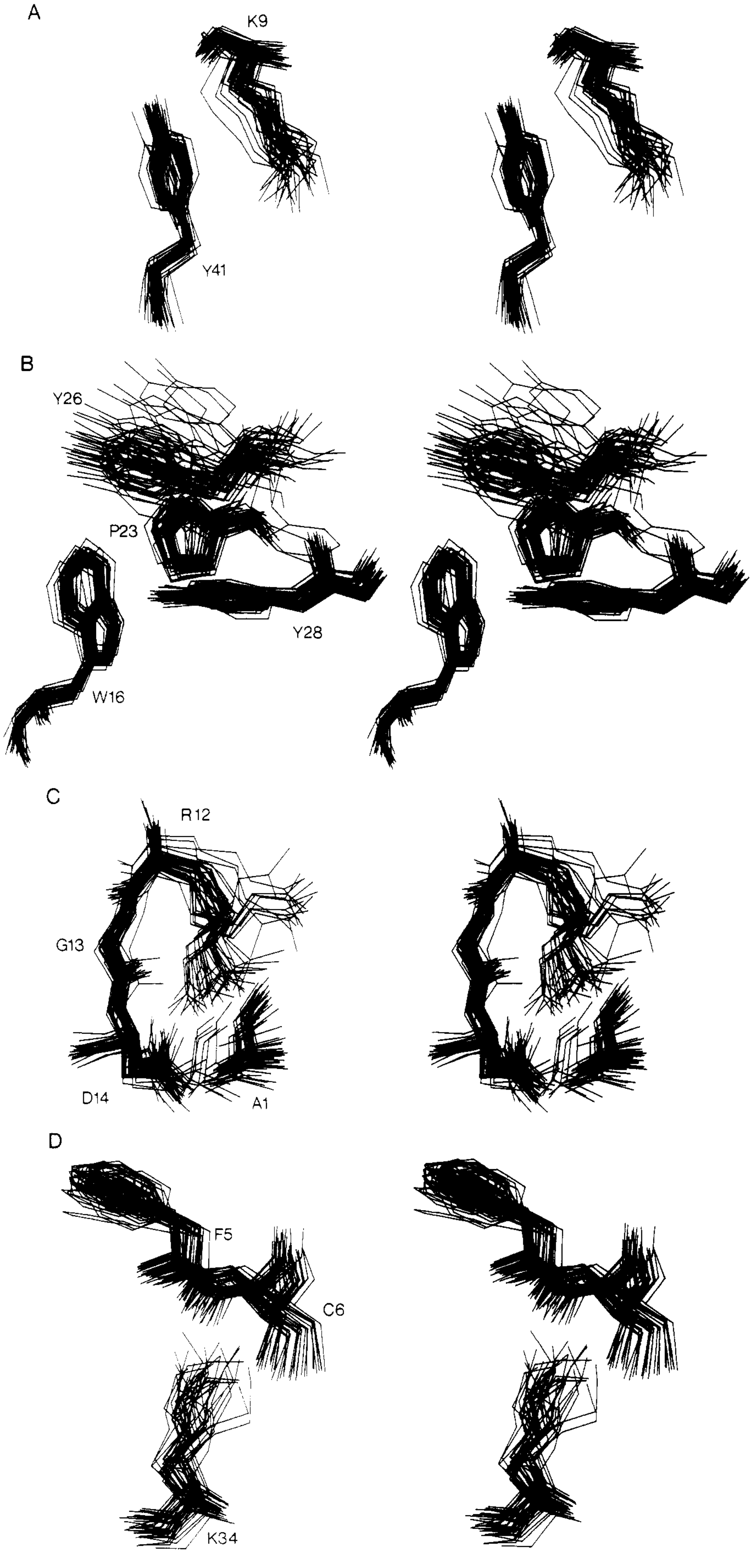

FIGURE 8: Stereoviews showing best fit superpositions of all atoms (excluding protons) of the 42 SA structures for four selected side-chain interactions. (A) Lys-9 and Tyr-41, (B) Trp-16, Pro-23, Tyr-26, and Tyr-28, (C) Ala-1, Arg-12, Gly-13, and Asp-14, and (D) Phe-5, Cys-6, and Lys-34.

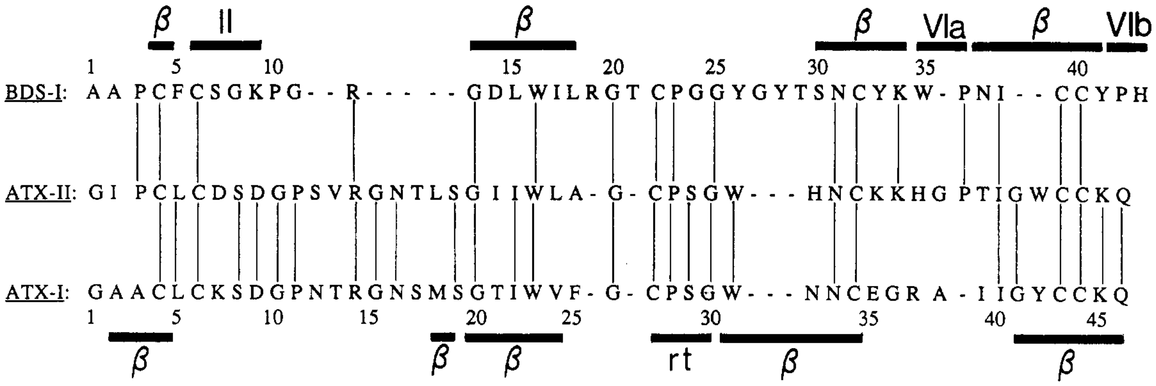

FIGURE 9: Sequence alignment of BDS-I with the toxins ATX-I and ATX-II based on their secondary structures determined by NMR (Driscoll et al., 1989; Widmer et al., 1988). The regions of secondary structure are indicated (β, extended β-strand; II, type II turn; VIa, type VIa turn; VIb, type VIb turn; rt, reverse turn).

structure. In general terms, these are largest for protons immediately adjacent to position 18, with diminishing effects as the spatial separation increases. No significant ring current shift effects due to the aromatic ring of Phe-18 can be discerned.

Structural Considerations for Sea Anemone Toxins. In the preceding paper (Driscoll et al., 1989) we highlighted the structural similarity of the β-sheet portions of BDS-I and the sea anenome toxins ATX-I and ATX-II from *Anemonia sulcata* (Widmer et al., 1988), AP-A from *Anthopleura xanthogrammica* (Gooley & Norton, 1986), and RP-II from *Radianthus paumotensis* (Wemmer et al., 1986). The sequence homologies between the toxins are greater than those between BDS-I and any one of them, so we shall restrict our comparisons to the ATX class only. The sequence alignment based on secondary structure shown in Figure 9 yields homologies of ~30% and ~21% with and without the cysteine residues, respectively, between BDS-I and the two ATX toxins. The corresponding values for ATX-I and ATX-II are 62% and 56%, respectively, suggesting that, in all likelihood, the two ATX toxins are isostructural. From Figure 9 it is clear that while BDS-I and the ATX toxins may share a common β-sheet fold, including the relative placement of the four cysteine residues involved in disulfide bridge formation in the core of the protein, the surrounding loop structures must be significantly different. Most striking is the substitution of the long loop of BDS-I (residues 17–30) by a six-residue segment that includes a reverse turn in ATX-I. Further, the N-terminal segment of the ATX-I protein which is not involved in β-sheet formation is longer than that in BDS-I. It is worth pointing out that the region identified as important for toxicity (Barhanin et al., 1981), namely, the pentapeptide segment Cys-(6)-Asp-X-Asp-Gly(10) containing the two conserved Asp residues in the toxins, is not part of the common β-sheet structure found in both the toxins and BDS-I. (Note that Asp-7 in ATX-I is replaced by a lysine and its toxicity is reduced by 50% relative to that of ATX-II.) In the case of BDS-I, both Asp-7 and Asp-9 are substituted by very different amino acid types, namely, Ser and Lys, respectively. This suggests that the detailed conformation of this part of the structure is quite different in BDS-I and the toxins and may explain the absence of toxicity for BDS-I. It therefore seems probable that the structural similarity of these proteins is limited to the basic fold, namely, the disulfide bridges and a section of β-sheet. A more detailed structural comparison will have to await the complete three-dimensional structures of the sea anemone toxins.

BDS-I also displays antiviral activity and has been shown to completely inhibit the cytopathic effects of mouse hepatitis virus strain MHV-A59 on mouse liver cells (Komoto and Beress, unpublished data). The mechanism by which this effect is mediated is unknown. It is interesting, however, to note the general similarity of the physical properties of BDS-I with the defensins, a class of small cationic polypeptides of 29–34 amino acid residues found in neutrophils which posess both antibacterial and antiviral activity (Selstead et al., 1983, 1985; Ganz et al., 1985; Leher et al., 1985; Daher et al., 1986). The defensins have three highly conserved disulfide bridges, arising from a distribution of cysteine residues in the primary sequence that is similar to that in BDS-I. A comparison of the three-dimensional structures of BDS-I and the defensins will therefore also be of interest. In this respect we note that crystals of a human defensin suitable for X-ray diffraction studies have been obtained (Stanfield et al., 1988).

CONCLUDING REMARKS

In this paper we have determined the three-dimensional structure of the antihypertensive and antiviral protein BDS-I for the sea anemone *Anemonia sulcata*. The use of stereospecific assignments and the collection of ^{1}H NMR data at 600 MHz have enabled us to obtain many more experimental restraints than has previously been possible for a protein of this size. The large number of structures, a total of 42, calculated by hybrid distance geometry–dynamical simulated annealing gives us confidence that the conformational space consistent with the experimental data has been thoroughly sampled. Both the backbone and side-chain positions, with only a few exceptions, are very well defined (Figures 2, 3, 4, and 7). This is achieved in spite of the fact that the NOE interproton distance restraints are only loosely classified into three broad distance ranges ($\leq$2.7 Å, $\leq$3.3 Å, and $\leq$5 Å), thus avoiding any potential problems associated with variable internal mobility and r^{-6} averaging. The success of obtaining such a well-defined structure is due to the fact that many of the distances are highly correlated and that short ($<$5 Å) distances between residues far apart in the sequence are conformationally restrictive even if they are only approximate. This is fortunate as accurate interproton distance measurements in proteins, particularly of those involving side chains, is likely to prove technically very difficult.

SUPPLEMENTARY MATERIAL AVAILABLE

One table giving the complete list of NOE interproton and hydrogen-bonding distance restraints and ϕ backbone and χ_1 side-chain torsion angle restraints used in the computation of the three-dimensional structure of BDS-I (13 pages). Ordering information is given on any current masthead page. The coordinates of the 42 SA structures and of the restrained minimized average structure $(\overline{SA})_r$ have been deposited in the Brookhaven Protein Data Bank.

Registry No. (Leu-18)-BDS-I, 96510-29-1; (Phe-18)-BDS-I, 118246-78-9.

REFERENCES

Barhanin, J., Hughes, M., Schweitz, H., Vincent, J. P., & Lazdunski, M. (1981) *J. Biol. Chem. 256*, 5764–5769.

Beress, L., Doppelfeld, I.-S., Etschenberg, E., Graf, E., Henschen, A., & Zwick, J. (1985) Federal Republic of Germany Patent DE 3324689 A1.

Billeter, M., Havel, T. F., & Wüthrich, K. (1987) *J. Comput. Chem. 8*, 132–141.

Braun, W., & Go, N. (1985) *J. Mol. Biol. 186*, 611–626.

Brooks, B. R., Bruccoleri, R. E., Olafson, B. D., States, D. J., Swaminathan, S., & Karplus, M. (1983) *J. Comput. Chem. 4*, 187–217.

Brünger, A. T. (1988) *J. Mol. Biol. 203*, 803–816.

Brünger, A. T., Clore, G. M., Gronenborn, A. M., & Karplus, M. (1986) *Proc. Natl. Acad. Sci. U.S.A. 83*, 3201–3805.

Brünger, A. T., Kuryan, J., & Karplus, M. (1987a) *Science 235*, 458–460.

Brünger, A. T., Clore, G. M., Gronenborn, A. M., & Karplus, M. (1987b) *Protein Eng. 1*, 399–406.

Chothia, C. (1973) *J. Mol. Biol. 75*, 295–302.

Chothia, C., Levitt, M., & Richardson, D. (1977) *Proc. Natl. Acad. Sci. U.S.A. 74*, 4130–4134.

Clore, G. M., & Gronenborn, A. M. (1987) *Protein Eng. 1*, 275–288.

Clore, G. M., Gronenborn, A. M., Brünger, A. T., & Karplus, M. (1985) *J. Mol. Biol. 186*, 435–455.

Clore, G. M., Nilges, M., Sukumaran, D. K., Brünger, A. T., Karplus, M., & Gronenborn, A. M. (1986a) *EMBO J. 5*, 2729–2735.

Clore, G. M., Brünger, A. T., Karplus, M., & Gronenborn, A. M. (1986b) *J. Mol. Biol. 191*, 523–551.

Clore, G. M., Sukumaran, D. K., Nilges, M., & Gronenborn, A. M. (1987a) *Biochemistry 26*, 1732–1745.

Clore, G. M., Gronenborn, A. M., Nilges, M., & Ryan, C. A. (1987b) *Biochemistry 26*, 8012–8023.

Clore, G. M., Gronenborn, A. M., Kjaer, M., & Poulsen, F. M. (1987c) *Protein Eng. 1*, 305–311.

Clore, G. M., Gronenborn, A. M., James, M. N. G., Kjaer, M., McPhalen, C. A., & Poulsen, F. M. (1987d) *Protein Eng. 1*, 313–318.

Daher, K. A., Selstead, M. E., & Leher, R. I. (1986) *J. Virol. 60*, 1068–1074.

Driscoll, P. C., Clore, G. M., Beress, L., & Gronenborn, A. M. (1989) *Biochemistry* (preceding paper in this issue).

Ganz, T., Selsted, M. E., Szklarek, D., Harwig, S. S. L., Daher, K. Bainton, F., & Lehere, R. I. (1985) *J. Clin. Invest. 76*, 1427–1435.

Gooley, P. R., & Norton, R. S. (1986) *Biochemistry 25*, 2349–2356.

Havel, T. F. (1986) DISGEO, Quantum Chemistry Program Exchange No. 507, Indiana University.

Havel, T. F., & Wüthrich, K. (1984) *Bull. Math. Biol. 45*, 673–698.

Havel, T. F., & Wüthrich, K. (1985) *J. Mol. Biol. 182*, 381–294.

Havel, T. F., Crippen, G. M., & Kuntz, I. D. (1979) *Biopolymers 18*, 73–81.

Havel, T. F., Kuntz, I. D., & Crippen, G. M. (1983) *Bull. Math. Biol. 45*, 665–720.

Kaptein, R., Zuiderweg, E. R. P., Scheek, R. M., Boelens, R., & van Gunsteren, W. F. (1985) *J. Mol. Biol. 182*, 179–182.

Kline, A. D., Braun, W., & Wüthrich, K. (1986) *J. Mol. Biol. 183*, 503–507.

Lehrer, R. I., Daher, K., Ganz, T., & Selsted, M. E. (1985) *J. Virol. 54*, 467–472.

Markley, J. L. (1975) *Acc. Chem. Res. 8*, 70–80.

Nilges, M., Clore, G. M., & Gronenborn, A. M. (1988a) *FEBS Lett. 229*, 317–324.

Nilges, M., Gronenborn, A. M., Brünger, A. T., & Clore, G. M. (1988b) *Protein Eng. 2*, 27–38.

Nilges, M., Clore, G. M., & Gronenborn, A. M. (1988c) *FEBS Lett. 239*, 129–136.

Pardi, A., Billeter, M., & Wüthrich, K. (1984) *J. Mol. Biol. 180*, 741–751.

Richardson, J. S. (1981) *Adv. Protein Chem. 34*, 167–339.

Schulz, G. E., & Schirmer, R. E. (1979) *Principles of Protein Structure*, Springer-Verlag, Berlin.

Selsted, M. E., Brown, D. M., Delange, R. J., & Lehrer, R. I. (1983) *J. Biol. Chem. 258*, 14485–14489.

Selsted, M. E., Harwig, S. S. L., Ganz, T., Schilling, J. W., & Lehrer, R. I. (1985) *J. Clin. Invest. 76*, 1436–1439.

Stanfield, R. L., Westbrook, E. M., & Selsted, M. E. (1988) *J. Biol. Chem. 263*, 5933–5935.

Wagner, G., Braun, W., Havel, T. F., Schaumann, T., Go, N., & Wüthrich, K. (1987) *J. Mol. Biol. 196*, 611–639.

Wemmer, D. E., Kumar, N. V., Metrione, R. M., Lazdunski, M., Drobny, G., & Kallenbach, N. R. (1986) *Biochemistry 25*, 6842–6849.

Widmer, A., Wagner, G., Schweitz, N., Lazdunski, M., & Wüthrich, K. (1988) *Eur. J. Biochem. 171*, 177–192.

Williamson, M. P., Havel, T. F., & Wüthrich, K. (1985) *J. Mol. Biol. 182*, 295–315.

Wunderer, G. (1978) *Hoppe-Seyler's Z. Physiol. Chem. 359*, 1193–1201.

Wüthrich, K. (1986) *NMR of Proteins and Nucleic Acids*, Wiley, New York.

Wüthrich, K., Billeter, M., & Braun, W. (1983) *J. Mol. Biol. 169*, 949–961.